

Various Models for Faults in Transmission Lines and Their Detection Using Time Domain Reflectometry

Laurent Sommervogel*

Abstract—This paper presents new ways of modelling several types of faults that can be encountered while monitoring cables throughout their lifecycle. These models comply with the traditional RLGC representation of a transmission line, which makes them easily usable for numerical simulations in frequency-domain. Theoretical fault signatures will then be extracted in time-domain to provide a better way of analyzing plots given by traditional devices, like time domain reflectometers (TDR). This allows a more accurate assessment of a cable’s health and condition. It will be shown in particular that some faults can be detected even if their damaged zone remains small compared to the wavelength. A direct benefit from this is that very expensive high frequency tools are not always necessary to detect these faults. The general objective of this paper is to improve fault location accuracy by combining measurement and simulation. It will be shown how this combination can become a powerful tool to detect, locate, and characterize a defect in a cable. The suggested models can be applied to any type of cable, from a coaxial line to a multi wire harness. In this work, a focus has been put on civil and military aircrafts, but similar cables are also found in cars or nuclear power plants for instance.

1. INTRODUCTION

Over the last decades, the exponential need for cables in modern systems has caused growing complexity of wired networks, especially in avionics. These cables can be exposed to aggressive environmental or operational conditions, leading to degradations and further serious consequences [1]. Reflectometry methods in time and/or frequency domain are the most commonly used for low-voltage wire diagnosis [2, 13]. Among them, we chose to focus our work on multi-carrier time domain reflectometry (MCTDR) [3]. The basic idea is that a fault in a cable will create at least one impedance mismatch at some point along the line, causing part of the incident wave to be reflected back to the injection point. This fault can either be qualified as *hard* in case of open/short circuit, or *soft* for any other damage. It is argued that the type of the fault (depending on the cable health and condition) will affect the shape of the echo, whatever the level of the fault’s severity. More precisely, this means that, under certain conditions, a soft fault could be detected even if it is arbitrarily small compared to the wavelength. It will also be proven that soft fault echoes not always result in a double-peak shape, although it could seem intuitive to associate two impedance mismatches to a soft fault (first one when ‘entering’ the fault, second one when ‘exiting’ the fault). But for some cases, a single impedance mismatch completely describes the phenomenon. Experimental validation will be conducted, and measurements will be compared with numerical simulations.

This paper is organized as follows. In Section 2, the formulation of the problem will be described. Section 3 presents a comparison between measurement campaigns and numerical simulations. Concluding remarks are given in Section 4.

Received 7 April 2020, Accepted 15 June 2020, Scheduled 28 June 2020

* Corresponding author: Laurent Sommervogel (laurent.sommervogel@win-ms.com).
The author is with the WiN-MS — 503, rue du Belvédère — 91400 Orsay, France.

2. THEORY AND ANALYSIS

2.1. Multiple Cables, Multiple Faults

Aircraft electrical wiring interconnection system (EWIS) mainly consists of copper or aluminum cables with polyamide or polyimide insulation. They can be bundled or not, twisted or not, shielded or not. Some of them used for radio navigation systems are high-frequency low-loss coaxial cables. Some others involved for overheat detection systems use eutectic salt as insulator, turning them into hot air leak locators [6]. That is why, depending on the type of cable, multiple kinds of faults can be encountered: open or short circuit of course, but also loose connection, moisture in connector, arc fault (series or parallel), metal corrosion, bad insulation (moisture in dielectric material), hot spot, excessive bending or crushing, chafing, or even slow deterioration caused by chemical alteration or ionizing radiation (e.g., cables exposed inside a nuclear power plant).

2.2. Propagation Mode

Many authors [1, 2, 7, 8] rely on a 4-parameter model (RLGC) to describe the propagation of a wave (with associated voltage V and current I) inside a cable, from which come the well-known telegrapher's equations [10].

R and L pertain to the cable's conductor, whilst C and G pertain to the cable's insulator. This 2-port network describes an elementary component of the transmission line, i.e., whose length dx is infinitely small. Let us recall that, based on this model, we define the characteristic impedance as a function of the angular frequency ω :

$$Z_c(\omega) = \sqrt{\frac{R + jL\omega}{G + jC\omega}} \quad (1)$$

and the propagation constant as well:

$$\gamma_c(\omega) = \sqrt{(R + jL\omega)(G + jC\omega)} = \alpha(\omega) + j\beta(\omega) \quad (2)$$

Finally, if there is an impedance variation along the line (e.g., from Z_{c1} to Z_{c2}), the local reflection coefficient is defined as follows [14]:

$$\Gamma = \frac{Z_{c2} - Z_{c1}}{Z_{c2} + Z_{c1}} \quad (3)$$

Whilst propagation in cables is widely known, what is happening throughout a fault is not so well described. Thereafter, analytical expressions of the fault's reflection coefficient (Γ_f) and transmission coefficient (τ_f) will be established for various types of faults.

Losses due to the fault can also be calculated. Indeed, if there was no fault, the law of conservation of energy states that the total power is the sum of the reflected power and the transmitted power:

$$|\Re|^2 + |\text{T}|^2 = 1 \quad (4)$$

where \Re and T are respectively the reflected and transmitted voltage coefficients. If we now consider the cable's characteristic impedance to be the same at each side of a fault, we simply have:

$$\Re = \Gamma_f \quad \text{and} \quad \text{T} = \tau_f \quad (5)$$

Therefore, the power loss due to the fault, representing the amount of dissipated power, which is neither reflected nor transmitted can be expressed. It has the general form:

$$|L_f|^2 = 1 - |\Gamma_f|^2 - |\tau_f|^2 \quad (6)$$

2.3. Intuitive Approach for Fault Modelling

It is often admitted [4, 5, 9, 12] that a correct way of modelling a fault consists in inserting a faulty version of the 2-port network described in Fig. 1 (R , L , G , C values are modified according to the fault's severity) into the healthy network. Cascading these three networks leads to the following impedance profile (Fig. 2).

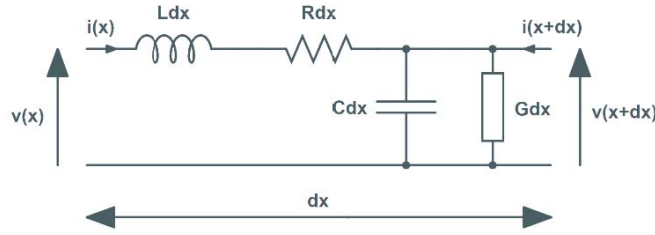


Figure 1. RLGC cable model.



Figure 2. Impedance profile for a change in RLGC parameters.

Taking a closer look at this kind of fault, it will actually create two impedance mismatches: one at each boundary of the fault (left then right). Using Equation (3), we can write:

$$\Gamma_{in} = \frac{Z_f - Z_c}{Z_f + Z_c} \quad \text{and} \quad \Gamma_{out} = \frac{Z_c - Z_f}{Z_c + Z_f} = -\Gamma_{in} \quad (7)$$

When the incident wave reaches the left boundary, the reflected voltage part is quantified by Γ_{in} and the transmitted voltage part by $1 + \Gamma_{in}$. There is an infinite number of bounces between the left and right boundaries of the fault, each one being delayed by $e^{-\gamma l}$, with l the length of the fault extension and γ the propagation constant inside the fault. Therefore, the global fault's reflection coefficient can be derived:

$$\begin{aligned} \Gamma_f &= \Gamma_{in} + (1 + \Gamma_{in}) e^{-\gamma l} (-\Gamma_{in}) e^{-\gamma l} (1 - \Gamma_{in}) + \dots \\ &= \Gamma_{in} - \Gamma_{in} (1 - \Gamma_{in}^2) e^{-2\gamma l} - \Gamma_{in}^3 (1 - \Gamma_{in}^2) e^{-4\gamma l} - \Gamma_{in}^5 (1 - \Gamma_{in}^2) e^{-6\gamma l} + \dots \\ &= \Gamma_{in} - \Gamma_{in} e^{-2\gamma l} + \Gamma_{in}^3 e^{-2\gamma l} - \Gamma_{in}^3 e^{-4\gamma l} + \Gamma_{in}^5 e^{-4\gamma l} - \Gamma_{in}^5 e^{-6\gamma l} + \Gamma_{in}^7 e^{-6\gamma l} \dots \\ &= \Gamma_{in} \left(1 - e^{-2\gamma l} \right) \left(1 + \Gamma_{in}^2 e^{-2\gamma l} + \Gamma_{in}^4 e^{-4\gamma l} + \dots \right) \end{aligned} \quad (8)$$

Since $|\Gamma_{in}| < 1$, this geometric series converges to:

$$\Gamma_f = \Gamma_{in} \frac{1 - e^{-2\gamma l}}{1 - \Gamma_{in}^2 e^{-2\gamma l}} \quad (9)$$

This is an other way of obtaining the result already given in [12] Eq. (6), which can be rewritten as in [4] Eq. (7):

$$\frac{\Gamma_f}{\Gamma_{in}} = \frac{2j e^{-j\beta l} \sin \beta l}{1 - \Gamma_{in}^2 e^{-2j\beta l}} \quad (10)$$

Alternative formalism like ABCD matrices [15] would also lead to the same result.

The same procedure can be conducted to derive the global fault's transmission coefficient:

$$\begin{aligned} \tau_f &= (1 + \Gamma_{in}) e^{-\gamma l} (1 - \Gamma_{in}) + \dots \\ &= (1 - \Gamma_{in}^2) e^{-\gamma l} + \Gamma_{in}^2 (1 - \Gamma_{in}^2) e^{-3\gamma l} + \dots \\ &= (1 - \Gamma_{in}^2) e^{-\gamma l} \left(1 + \Gamma_{in}^2 e^{-2\gamma l} + \Gamma_{in}^4 e^{-4\gamma l} + \dots \right) \end{aligned} \quad (11)$$

which also converges to:

$$\tau_f = \frac{1 - \Gamma_{in}^2}{1 - \Gamma_{in}^2 e^{-2\gamma l}} e^{-\gamma l} \quad (12)$$

The power loss due to the fault can now be computed using Eq. (6). For the sake of simplicity, let us consider first order expansions and real values for impedances:

$$\begin{aligned} |L_f|^2 &\approx 1 - \Gamma_{\text{in}}^2 - (1 - \Gamma_{\text{in}}^2)^2 e^{-2\alpha l} \\ &\approx (1 - \Gamma_{\text{in}}^2) \left(1 - e^{-2\alpha l}\right) \end{aligned} \quad (13)$$

It clearly appears that if the length of the fault is zero, obviously there is no loss. On the other hand, power loss can never exceed $1 - \Gamma_{\text{in}}^2$.

It has been widely discussed [4, 5] that, in time-domain, Eq. (9) leads to specific double-peak echoes resulting from impulse probe signals. Obviously this shape differs from an open circuit (single positive peak) or a short circuit (single negative peak), which means that a hard fault cannot be considered as an extreme scenario of a soft fault when relying on this model.

As it will be shown later with experimental validation, this model is in fact only accurate for faults having a non-zero spatial extension. This encompasses bending or crushing issues, chafing or damaged shielding, chemical degradation or radiation. But this model lacks to describe what happens with moisture inside a connector, arc fault, hot spot, insulation fault ...

2.4. Alternative Modelling for a Series Fault

The following model (Fig. 3) aims at describing a lumped series fault, i.e., having no spatial extension or one being arbitrary small compared to the wavelength.

This applies very well to moisture inside a connector or series arc.

At the fault's location, the local characteristic impedance is actually increased by the impedance of the fault. The global fault's reflection coefficient is directly derived from this mismatch:

$$\Gamma_f = \frac{(Z_f + Z_c) - Z_c}{(Z_f + Z_c) + Z_c} = \frac{Z_f}{Z_f + 2Z_c} \quad (14)$$

Z_f can be either purely real (like the lumped resistor depicted in Fig. 3) or complex as well.



Figure 3. Impedance profile for a lumped series resistive fault.

This time, the global fault's transmission coefficient can *not* be found using $1 + \Gamma_f$, as this relation generally holds for cascaded transmission lines with identical characteristic impedances. So it is required to derive it from the voltages and currents at the left (V_l, I_l) and the right (V_r, I_r) sides of the fault:

$$\begin{aligned} \tau_f &= \frac{V_r - Z_c I_r}{V_l + Z_c I_l} = \frac{V_l - Z_f I_l + Z_c I_l}{V_l + Z_c I_l} \\ &= \frac{(Z_f + Z_c) - Z_f + Z_c}{(Z_f + Z_c) + Z_c} = \frac{2Z_c}{Z_f + 2Z_c} = 1 - \Gamma_f \end{aligned} \quad (15)$$

Considering real values for impedances, power loss due to the fault can be easily calculated using Eq. (6):

$$L_f^2 = 1 - \left(\frac{Z_f}{Z_f + 2Z_c}\right)^2 - \left(\frac{2Z_c}{Z_f + 2Z_c}\right)^2 = \frac{4Z_c Z_f}{(Z_f + 2Z_c)^2} \quad (16)$$

And then two extreme cases are worth noticing:

$$\begin{aligned} Z_f \ll Z_c &\Rightarrow L_f^2 \approx \frac{Z_f}{Z_c} \\ Z_f \gg Z_c &\Rightarrow L_f^2 \approx 4 \frac{Z_c}{Z_f} \end{aligned} \quad (17)$$

In time domain, Eq. (14) leads to positive single-peak echoes resulting from impulse probe signals. Considering the extreme scenario of an open circuit ($Z_f \rightarrow +\infty$), we have:

$$\begin{aligned} \lim_{Z_f \rightarrow +\infty} \Gamma_f &= +1 \\ \lim_{Z_f \rightarrow +\infty} \tau_f &= 0 \end{aligned} \tag{18}$$

which is actually consistent: all the energy is reflected back when reaching an open circuit, and none is travelling through. It is worth noticing from Eq. (17) that whether the fault impedance is zero (no fault) or high (open circuit), obviously there is no loss.

2.5. Alternative Modelling for a Parallel Fault

The following model (Fig. 4) aims at describing a lumped parallel fault (still no spatial extension).

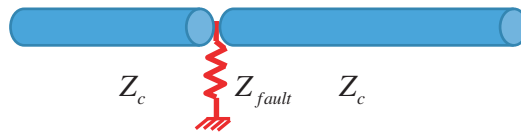


Figure 4. Impedance profile for a lumped parallel resistive fault.

This applies very well to insulation fault (conductive leak for example), hot spot or parallel arc.

Here, the fault impedance is put in parallel with the local characteristic impedance. Once more, this creates a mismatch from which the global fault’s reflection coefficient is directly derived:

$$\Gamma_f = \frac{\frac{Z_f Z_c}{Z_f + Z_c} - Z_c}{\frac{Z_f Z_c}{Z_f + Z_c} + Z_c} = \frac{-Z_c}{2Z_f + Z_c} \tag{19}$$

Likewise, Z_f can be real (like the lumped resistor depicted in Fig. 4) or complex. If we rewrite Eq. (19) as follows:

$$\Gamma_f = \frac{-1}{1 + 2\frac{Z_f}{Z_c}} \tag{20}$$

we obtain the result given in [6], Section 3.

Again, it is required to derive the global fault’s transmission coefficient from the voltages and currents at each side of the fault:

$$\tau_f = \frac{V_r - Z_c I_r}{V_l + Z_c I_l} = \frac{2\frac{Z_f Z_c}{Z_f + Z_c}}{\frac{Z_f Z_c}{Z_f + Z_c} + Z_c} = \frac{2Z_f}{2Z_f + Z_c} = 1 + \Gamma_f \tag{21}$$

Considering real values for impedances, power loss due to the fault is calculated using Eq. (6) as follows:

$$L_f^2 = 1 - \left(\frac{-Z_c}{2Z_f + Z_c}\right)^2 - \left(\frac{2Z_f}{2Z_f + Z_c}\right)^2 = \frac{4Z_c Z_f}{(2Z_f + Z_c)^2} \tag{22}$$

Then we could also consider these two extreme cases:

$$\begin{aligned} Z_f \ll Z_c &\Rightarrow L_f^2 \approx 4\frac{Z_f}{Z_c} \\ Z_f \gg Z_c &\Rightarrow L_f^2 \approx \frac{Z_c}{Z_f} \end{aligned} \tag{23}$$

In time domain, Eq. (19) leads to negative single-peak echoes resulting from impulse probe signals. Considering the extreme scenario of a short circuit ($Z_f \rightarrow 0$), we have:

$$\begin{aligned}\lim_{Z_f \rightarrow 0} \Gamma_f &= -1 \\ \lim_{Z_f \rightarrow 0} \tau_f &= 0\end{aligned}\tag{24}$$

which is consistent: all the energy is reflected back (out of phase) when reaching a short circuit, and none is travelling through. It is worth noticing from Eq. (23) that whether the fault impedance is high (no fault) or zero (short circuit), obviously there is no loss.

3. EXPERIMENTAL VALIDATION

Three measurement campaigns have been conducted, one for each model. Numerical simulations have been performed thanks to an in-house code solving telegrapher's equations in the frequency domain and using Eqs. (9), (14), and (19) respectively. RLGC parameters follow Eq. (25) in the simulation code, so that the dispersion phenomenon is correctly taken into account [11].

$$\begin{aligned}R &= R_0 \sqrt{f} \quad \text{and} \quad G = G_0 f \\ L &= L_0 + \frac{R_0}{2\pi\sqrt{f}} \quad \text{and} \quad C = C_0\end{aligned}\tag{25}$$

R_0 , L_0 , C_0 , and G_0 are different for every cable's type and are estimated using genetic algorithms (GA). In the following experiments, 3 types of cables will be used. Their parameters obtained from the GA optimizations are recorded in the following Table 1.

Table 1. Parameters of cables used for the experiments.

Cable family	R_0	L_0	C_0	G_0
RG-58	130 $\mu\Omega/\text{m}$	250 nH/m	100 pF/m	0.8 pS/m
EN2714-013 MLA22	200 $\mu\Omega/\text{m}$	120 nH/m	300 pF/m	32 pS/m
NGR1-124A3-400	1300 $\mu\Omega/\text{m}$	220 nH/m	420 pF/m	1 pS/m

Measurements and simulations will be compared for each one of the three measurement campaigns.

3.1. Chafing Issue

A 50 Ω RG-58 coaxial cable has been used for the first experiment. The velocity of propagation (VoP) for this cable is approximately $0.66c$ (where c denotes the speed of light in vacuum). A soft fault was created by partially removing the outer sheath over a distance of 3 cm (Fig. 5), 0.98 m away from the injection point. The shield was left untouched. This fault typically represents a chafing issue in an aircraft. A wideband probe signal consisting of sine waves whose frequency is swept from 150 kHz to 6 GHz was used for the test. Upper frequency is significantly higher than the typical operating frequency of this cable, making the shield less effective and the fault apparent.

Due to the nature of the fault, the first model is used for the numerical simulation, with corresponding Eqs. (7) and (9). The following plot (Fig. 6) is obtained when setting Z_f to 55 Ω .

One can point out the excellent agreement between simulation and measurement. Thanks to the numerical simulation, it is safe to assume that the fault's severity actually is 55 Ω . One could argue that the impedance is gradually changing, considering the geometry of the defect. So it is more rigorous to refer to this severity as an equivalent fault impedance. Still, the value of 55 Ω is within 10% of the cable's nominal impedance. Thus, depending on the end-user application, this cable could be considered as healthy or not.



Figure 5. Chafing soft fault created on RG-58 coax cable.

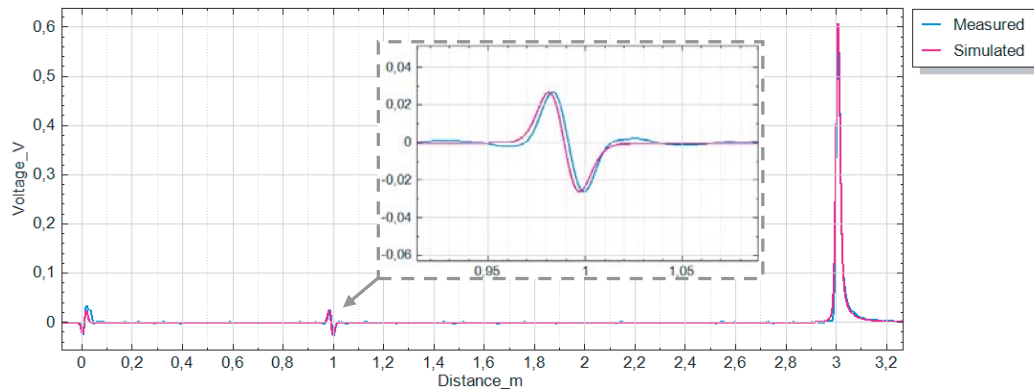


Figure 6. Measurement vs. simulation for chafing soft fault.



Figure 7. Typical cables used for OHDS system in an aircraft.

For the next two experiments, a typical setup (Fig. 7) used in modern aircrafts regarding overhear detection system (OHDS) [6] is considered. It consists of a $20\ \Omega$ EN2714-013 MLA22 shielded cable connected to a $25\ \Omega$ NGR1-124A3-400 sensing element. VoP for both cables are approximately $0.57c$ and $0.32c$ respectively. Two different soft faults will be studied: in Section 3.2, some water was introduced inside the connection to produce moisture and in Section 3.3, a hot spot was created using a hot air blower at nearly 200°C . Because these cables suffer from high dielectric loss, the MCTDR probe signal [3] that was used for both tests consisted of a sum of sine waves (sent all at once) ranging from a few kHz to no more than 50 MHz.

3.2. Moisture Inside Connectors

The connectors are soaked in a bucket of water (Fig. 8). The cumulated length of the connectors is only 5.5 cm. Assuming moisture spreads across the whole connection, the ratio l/λ cannot exceed 3%.

According to paper [5], the magnitude of the reflection is expected to be so small that it will be indistinguishable from the measurement noise (in these experiments, cables are considered ‘offline’ so that noise only refers to measurement noise, and not system noise). However, multiple meaningful reflectograms (Fig. 9) have been recorded over a total duration of 24 h.



Figure 8. Water-induced soft fault — moisture in connectors.

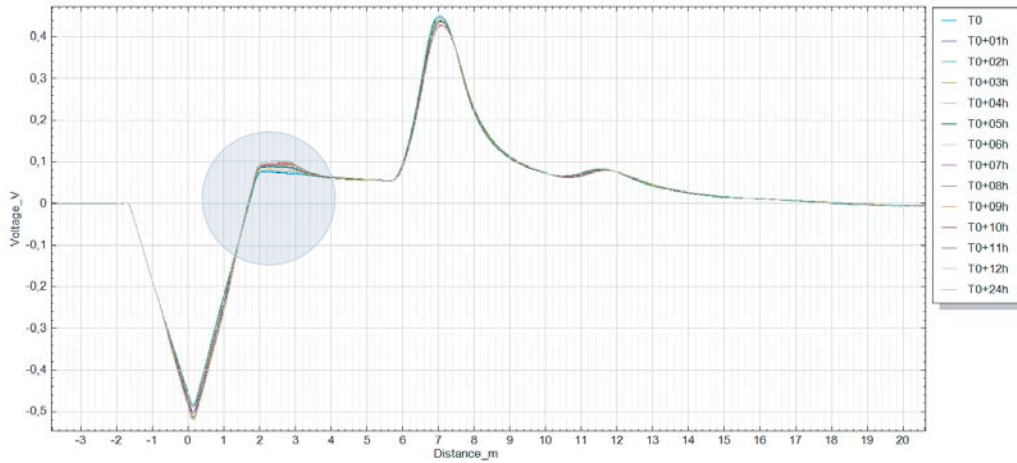


Figure 9. Reflectograms acquired during 24 h in water.

The X -axis origin is chosen so that when the measurement device is left open, the maximum of the output pulse is located at 0 m. This also applies to Figs. 11, 15, 16.

Not only can we see a positive single-peak signature at the junction's location (around 2 m), but also the fault's severity increases with time (Fig. 10).

As a result of these observations, the 2nd model (lumped series fault) has been used for the numerical simulation, with corresponding Eq. (14). The following plot is obtained when varying Z_f from 0Ω to 10Ω .

The same plot can be seen in Fig. 12 when zooming at the junction's location.

The curves coming from the measurement (Figs. 9, 10) have quite the same aspect as those from the simulation (Figs. 11, 12). Using a macro as an add-on to the in-house simulation software, the value of Z_f was then automatically tuned and retrieved when the simulated fault's magnitude matches the measured one for each measurement.

It is therefore possible to obtain a plot of fault's severity vs. time (Fig. 13). As it turns out, the fault's severity seems to follow an exponential law of the form:

$$Z_f(t) = Z_{f\infty} \left(1 - e^{-t/t_1}\right) \quad (26)$$

where $Z_{f\infty}$ is the asymptotic value and t_1 the time constant. Using a simple curve fitting algorithm, it has been subsequently established that taking $Z_{f\infty} = 4 \Omega$ and $t_1 = 8$ h gives a very high coefficient of determination of 0.97.

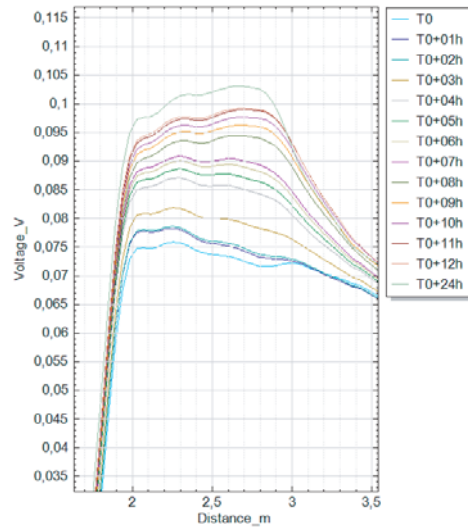


Figure 10. Zoom at junction’s location (same as Fig. 9).

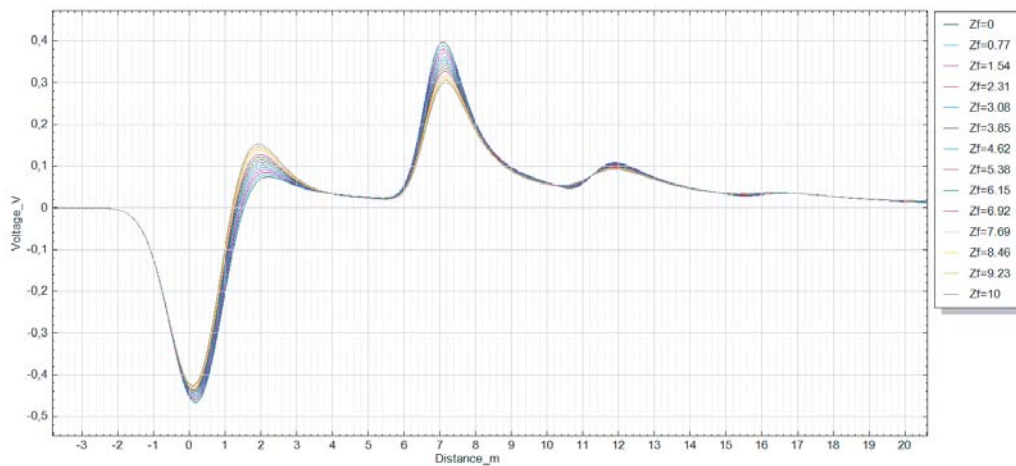


Figure 11. Numerical simulation for water-induced soft fault.

3.3. Hot Spot

Going back to the healthy setup depicted in Fig. 7, some hot air is now blown right in contact with the sensing element using a 350 W Steinel compact heat gun (Fig. 14). Inner cable’s temperature is expected to reach 200°C. The hot spot will be created at approximately half the length of the sensing element, i.e., 4.5 m away from the injection point.

Multiple reflectograms (Fig. 15) have been recorded over a total duration of 42 s.

Not only can we see a negative single-peak signature at the hot spot’s location (around 4.5 m), but also the fault’s severity increases with time (thus with temperature).

As a result of these observations, the 3rd model (lumped parallel fault) has been used for the numerical simulation, with corresponding Eq. (19). The following plot is obtained when varying Z_f from 1 Ω down to 4 Ω.

In this case too, a high degree of similarity is observed between the curves coming from the measurement (Fig. 15) and those from the simulation (Fig. 16). As described above (Z_f tuning), the law is this time assumed to be an exponential decay (Fig. 17):

$$Z_f(t) = Z_{f0}e^{-(t-t_0)/t_2} \tag{27}$$

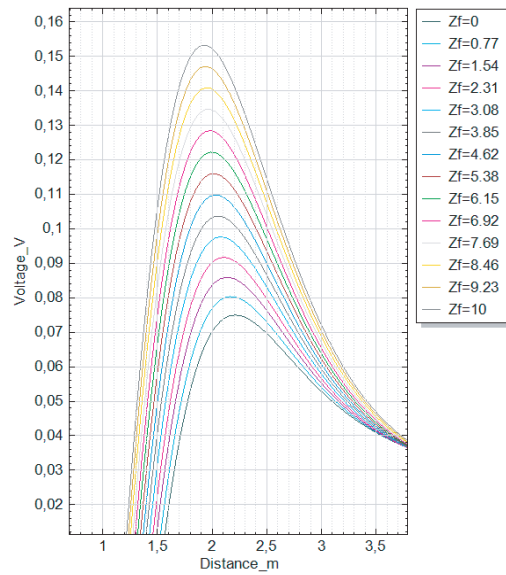


Figure 12. Zoom at junction's location (same as Fig. 11).

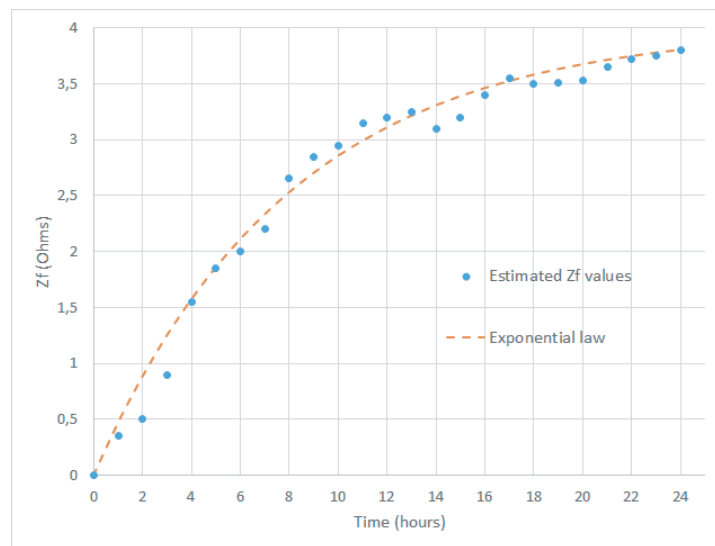


Figure 13. Moisture severity (fault's impedance) vs. time



Figure 14. Heat-induced soft fault: hot spot in sensing element.

where t_0 is the time it takes for the eutectic salt to start melting, Z_{f0} the impedance value at that time (isolation resistance), and t_2 the time constant. An excellent coefficient of determination of 0.98 is also found when taking $t_0 = 10$ s, $Z_{f0} = 1$ k Ω and $t_2 = 5$ s (curve fitting algorithm).

As mentioned in [6], if the relationship between Z_f and temperature is known, then it becomes possible to estimate temperature along the cable.

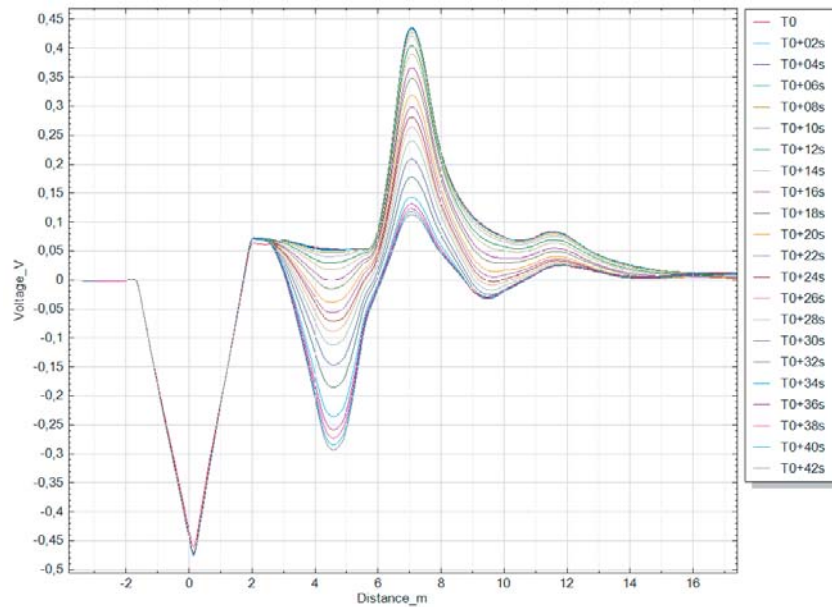


Figure 15. Reflectograms acquired during 42 s in hot air.

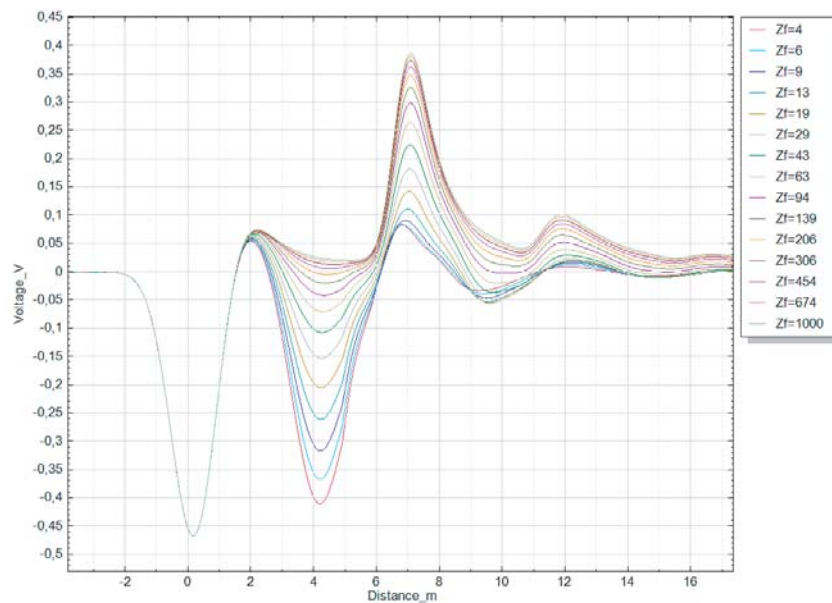


Figure 16. Numerical simulation for heat-induced soft fault.

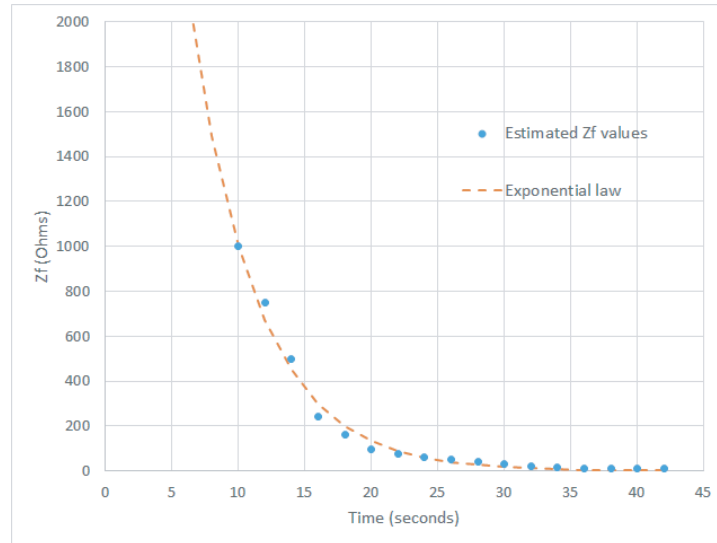


Figure 17. Hot spot severity (fault’s impedance) vs. time.

4. CONCLUSION

In this paper, we have presented various faults that may happen in an aircraft and how to model them. We also described the shape of the resulting echoes that could be observed when using reflectometer devices. More specifically, three models of soft faults (cascaded transmission lines, lumped series impedance, and lumped parallel impedance) have been validated through three experiments (chafing, moisture, and hot spot respectively). The test results have shown the accuracy of this new approach to model a lot of different faults, especially soft ones. With the help of numerical simulation, the characterization and location of a defect can be enhanced. It has been proven that soft fault echoes not always result in a double-peak shape. That is the main reason why in some cases, they can still be detectable even if the damaged zone is much smaller than the wavelength. This makes cheaper lower frequency devices as effective in detecting them as expensive laboratory tools, reducing the cost and time of avionics maintenance.

REFERENCES

1. Wheeler, K. R., D. A. Timucin, I. X. Twombly, K. F. Goebel, and P. F. Wysocki, “Aging aircraft wiring fault detection survey,” NASA Ames Research Center, CA 94035, 2007.
2. Auzanneau, F., “Wire troubleshooting and diagnosis: Review and perspectives,” *Progress In Electromagnetics Research B*, Vol. 49, 253–279, 2013.
3. Lelong, A. and M. O. Carrion, “On line wire diagnosis using multi-carrier time domain reflectometry,” *IEEE Sensors Conference*, 751–754, Christchurch, New Zealand, 2009.
4. Cozza, A. and L. Pichon, “Echo response of faults in transmission lines: Models and limitations to fault detection,” *IEEE Transactions on Microwave Theory and Techniques*, Vol. 64, No. 12, 4155–4164, 2016.
5. Griffiths, L. A., R. Parakh, C. Furse, and B. Baker, “The invisible fray: A critical analysis of the use of reflectometry for fray location,” *IEEE Sensors Journal*, Vol. 6, No. 3, 697–706, 2006.
6. Sallem, S., L. Sommervogel, M. Olivas, and A. Peltier, “Method and device for hot air leak detection in aircraft installation by wire diagnosis,” *IEEE AUTOTESTCON*, 1–6, 2016.
7. Loëte, F., S. Noël, M. O. Carrion, and F. Auzanneau, “Feasibility of the detection of vibration induced faults in connectors by reflectometry,” *ICEC 24th*, 2008.

8. Tang, H. and Q. Zhang, "An inverse scattering approach to soft fault diagnosis in lossy electric transmission lines," *IEEE Transactions on Antennas and Propagation*, Vol. 59, No. 10, 3730–3737, 2011.
9. Franchet, M., M. Olivas, N. Ravot, and L. Sommervogel, "Modelling the effect of a defect on crosstalk signals under the weak coupling assumption," *PIERS Proceedings*, 119–123, Xi'an, China, March 22–26, 2010.
10. Hayt, W. H. and J. A. Buck, *Engineering Electromagnetics*, 8th edition, 305–307, McGraw-Hill, 2012.
11. Zhang, J., Q. B. Chen, Z. Qiu, J. L. Drewniak, and A. Orlandi, "Extraction of causal RLGC models from measurements for signal link path analysis," *ISEC EMC*, 1–6, 2008.
12. Schuet, S., D. Timuçin, and K. Wheeler, "A model-based probabilistic inversion framework for characterizing wire fault detection using TDR," *IEEE TIM*, Vol. 60, No. 5, 1654–1663, 2011.
13. Shin, Y. J., J. Powers, T. S. Choe, C. Y. Hong, E. S. Song, J. G. Yook, and J. B. Park, "Application of time-frequency domain reflectometry for detection and localization of a fault on a coaxial cable," *IEEE TIM*, Vol. 54, No. 6, 2493–2500, 2005.
14. Paulter, N. G., "An assessment on the accuracy of time-domain reflectometry for measuring the characteristic impedance of transmission line," *IEEE TIM*, Vol. 50, No. 5, 1381–1388, 2001.
15. Zhang, Q., N. Berrabah, M. Franchet, and D. Vautrin, "De-embedding unmatched connectors for electric cable fault diagnosis," *IFAC*, Vol. 51, 1439–1444, 2018.